Harnessing the interface mechanics of hard films and soft substrates for 3D assembly by controlled buckling

Yuan Liu[a,b,1], Xueju Wang[c,1], Yameng Xu[d], Zhaoguo Xue[a,b], Yi Zhang[e], Xin Ning[f], Xu Cheng[a,b], Yeguang Xue[g,h], Di Lu[i], Qihui Zhang[d], Fan Zhang[a,b], Jianxing Liu[a,b], Xiaogang Guo[a,b], Keh-Chih Hwang[a], Yonggang Huang[d,g,h,i,j,2], John A. Rogers[d,g,h,i,j,k,l,m,2], and Yihui Zhang[a,b,2]

[a]Applied Mechanics Laboratory, Department of Engineering Mechanics, Tsinghua University, 100084 Beijing, P.R. China; [b]Center for Flexible Electronics Technology, Tsinghua University, 100084 Beijing, P.R. China; [c]Department of Mechanical and Aerospace Engineering, University of Missouri, Columbia, MO 65211; [d]Department of Materials Science and Engineering, Northwestern University, Evanston, IL 60201; [e]Department of Biomedical, Biological, and Chemical Engineering, University of Missouri, Columbia, MO 65211; [f]Department of Aerospace Engineering, Pennsylvania State University, State College, PA 16803; [g]Department of Mechanical Engineering, Northwestern University, Evanston, IL 60208; [h]Department of Civil and Environmental Engineering, Northwestern University, Evanston, IL 60208; [i]Center for Bio-Integrated Electronics, Northwestern University, Evanston, IL 60208; [j]Department of Chemistry, Northwestern University, Evanston, IL 60208; [k]Department of Biomedical Engineering, Northwestern University, Evanston, IL 60208; [l]Department of Neurological Surgery, Northwestern University, Evanston, IL 60208; and [m]Department of Electrical Engineering and Computer Science, Northwestern University, Evanston, IL 60208

Contributed by John A. Rogers, June 11, 2019 (sent for review May 6, 2019; reviewed by Pedro M. Reis and Yong Zhu)

Techniques for forming sophisticated, 3D mesostructures in advanced, functional materials are of rapidly growing interest, owing to their potential uses across a broad range of fundamental and applied areas of application. Recently developed approaches to 3D assembly that rely on controlled buckling mechanics serve as versatile routes to 3D mesostructures in a diverse range of high-quality materials and length scales of relevance for 3D microsystems with unusual function and/or enhanced performance. Nonlinear buckling and delamination behaviors in materials that combine both weak and strong interfaces are foundational to the assembly process, but they can be difficult to control, especially for complex geometries. This paper presents theoretical and experimental studies of the fundamental aspects of adhesion and delamination in this context. By quantifying the effects of various essential parameters on these processes, we establish general design diagrams for different material systems, taking into account 4 dominant delamination states (wrinkling, partial delamination of the weak interface, full delamination of the weak interface, and partial delamination of the strong interface). These diagrams provide guidelines for the selection of engineering parameters that avoid interface-related failure, as demonstrated by a series of examples in 3D helical mesostructures and mesostructures that are reconfigurable based on the control of loading-path trajectories. Three-dimensional micromechanical resonators with frequencies that can be selected between 2 distinct values serve as demonstrative examples.

3-dimensional assembly | buckling | interface mechanics | reconfigurable 3D structures

Complex 3D mesostructures that incorporate high-performance functional materials are of emerging importance in advanced electronic/optoelectronic devices (1–3), microelectromechanical systems (MEMS) (4, 5), photonic components (6, 7), bio-integrated sensors (8–12), and energy storage platforms (13–15). As a consequence, methods for customized manufacture of such classes of sophisticated 3D mesostructures are of increasing interest. Techniques for these purposes can be categorized into direct-type 3D fabrication (16–21) and indirect-type 3D assembly (22–31) schemes, each with advantages and limitations. Of the latter, those based on controlled, in- and out-of-plane buckling of preformed 2D structures provide high levels of versatility in engineering design (22, 32–38). Key attractive features include access to a broad range of structure layouts and feature sizes enabled by processes of 2D-to-3D transformation and full compatibility with state-of-the-art planar technologies adopted from the semiconductor and photonics industries. Recent publications demonstrate that these buckling-guided approaches represent powerful means for designing and forming 3D microsystems with unusual function and/or enhanced performance (39–42). Here, hard, patterned 2D structures, including those that support various functional materials and devices, serve as precursors that mount onto prestrained elastomeric substrates. Covalent bonds at strategic locations of the hard/soft interface between the precursor and the substrate form sites of strong adhesion, while the other regions are governed by relatively weak van der Waals interactions (22). Release of the prestrain induces delamination at the weak interfaces, such that lateral buckling of 2D precursor films ensues upon release of the prestrain, resulting in controlled transformation into a corresponding 3D structure. Undesired interface behaviors, either in the form of a partial delamination of the weak interface or delamination of the strong interface, can lead to the formation of 3D systems with poorly controlled geometries (3, 22, 43). A clear, quantitative understanding of the interface mechanics in this hard/soft system is, therefore, essential to reliable control over the assembly process.

Significance

The 3D micro and nanostructures in advanced materials serve as the basis for emerging classes of 3D microsystems that have unusual function and/or enhanced performance, with potential applications in biomedical devices, energy storage systems, and elsewhere. The results presented here establish a fundamental understanding of various aspects of interface mechanics associated with routes to such 3D systems that exploit concepts similar to those in pop-up books, thereby allowing the construction of general design diagrams. Findings also indicate that these principles in interface mechanics can provide the basis for 3D mesostructures with reconfigurable geometries of relevance to morphing microdevices, such as micromechanical resonators, antennas, and optical modulators.

Author contributions: Y.H., J.A.R., and Yihui Zhang designed research; Y.L., X.W., Y. Xu, Z.X., Yi Zhang, X.N., X.C., Y. Xue, D.L., Q.Z., F.Z., J.L., and X.G. performed research; Y.L., X.W., X.N., K.-C.H., Y.H., J.A.R., and Yihui Zhang analyzed data; and Y.L., X.W., Y.H., J.A.R., and Yihui Zhang wrote the paper.

Reviewers: P.M.R., École Polytechnique Fédérale de Lausanne; and Y.Z., North Carolina State University.

The authors declare no conflict of interest.

[1]Y.L. and X.W. contributed equally to this work.

[2]To whom correspondence may be addressed. Email: y-huang@northwestern.edu, jrogers@northwestern.edu, or yihuizhang@tsinghua.edu.cn.

This article contains supporting information online at www.pnas.org/lookup/suppl/doi:10.1073/pnas.1907732116/-/DCSupplemental.

Published online July 17, 2019.

Several published theoretical and experimental studies examined the mechanisms of wrinkling and delamination of hard films on soft substrates, when subjected to external compression. For example, Yu et al. (44) and Parry et al. (45) showed that substrate deformations have a significant effect on the buckling-driven delamination of thin films. Goyal et al. (46) and Mei et al. (47) studied the evolution of periodic wrinkling and localized delamination of thin films on soft substrates. Through combined theoretical and experimental approaches, Vella et al. (48, 49), Oshri et al. (50), and Zhang et al. (51) developed simple analytic solutions that can predict the evolution of buckling-driven delamination. Pan et al. (52) and Boijoux et al. (53) adopted cohesive models to simulate nonlinear delamination processes. Despite this important progress, these models do not apply directly to the mechanisms of geometric evolution that accompany interface delamination in buckling-guided 3D assembly, where hard/soft systems with complex geometries and the coexistence of weak and strong interfaces are intrinsic, essential features of the system.

The purpose of this work is 2-fold. First, we construct general design diagrams to guide the selection of parameters that avoid interface-related failure modes (i.e., partial delamination of the weak interface or delamination of the strong interface) in the 3D assembly, through combined theoretical and experimental studies. An interesting finding in this context is that the evolution of delamination length at the weak interface is highly insensitive to the location of the crack initiation. Second, we develop a design concept that actively harnesses the interface properties to achieve reconfigurable 3D mesostructures through control of the loading path, i.e., the time sequence of strain applied to the elastomer substrate. This strategy has wide applicability in the design and fabrication of reconfigurable 3D mesostructures in ways that are

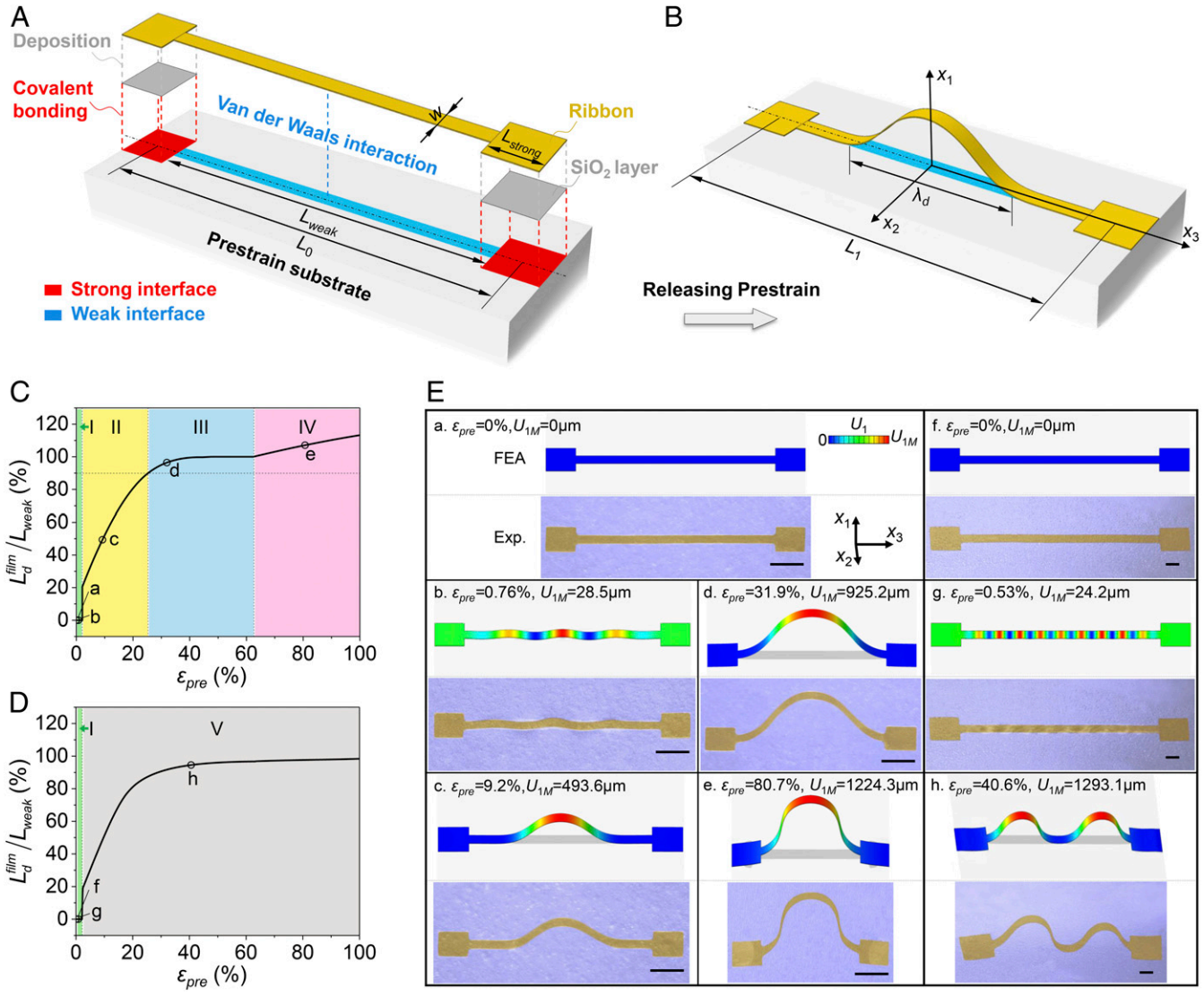

Fig. 1. Delamination processes associated with buckling-guided assembly of 3D mesostructures from 2D precursors. (*A* and *B*) Computational model associated with finite element analyses of straight ribbon mesostructures that include both strong and weak interfaces. (*C*) Delamination ratio (L_d^{film}/L_{weak}) versus prestrain (ε_{pre}) for a representative case (L_{weak} = 3 mm; h_f = 10 μm) with a single region (wave) of delamination. Four stages are identified, including wrinkling (regime I), partial delamination of the weak interface (regime II), full delamination of the weak interface (regime III), and partial delamination of the strong interface (regime IV). (*D*) Similar results for the case of delamination with 2 separated waves, in which, 2 different stages, wrinkling (regime I) and double-arc delamination of the weak interface (regime V) occur. Here, L_{weak} = 8 mm and h_f = 10 μm. (*E*) Representative in situ optical (colorized) images and FEA predictions corresponding to the states marked by *a*–*e* in *C* and *f*–*h* in *D*. (Scale bars, 500 μm.)

more scalable than those reported previously (32), where preformed creases with substantially reduced width or thickness at specific local regions of precursors are often required to achieve the structural bistability (32). As a demonstrative example of the ideas presented here, we describe a reconfigurable MEMS device whose resonance frequency can be adjusted between 2 distinct values.

Results and Discussion

Interface Mechanics of Buckling-Guided 3D Assembly of Straight Ribbon Structures. Fig. 1 describes the general process of interface delamination during 3D assembly, and the associated deformation modes for the simple case of a straight ribbon precursor. Fig. 1 *A* and *B* present the corresponding model for finite element analyses (FEA; see *Methods* for details) that takes into account the progressive separation of both the weak and strong film-substrate interfaces. The weak interface is dominated by van der Waals interactions associated with contact of the film to the substrate, while the strong interface is governed by covalent chemical bonding created by interfacial condensation reactions between hydroxyl surface chemistry on a SiO_2 layer patterned at the bottom side of the film and that on the UV–ozone-treated surface of the silicone substrate (see *SI Appendix*, Fig. S1, for details about the fabrication process). Cohesive zone models with a simple bilinear constitutive law govern simulations of the delamination processes at different interfaces associated with wrinkling and buckling of the film upon release of the prestrain in the substrate. The interface energy (γ) and interface strength (T_1^0) in the cohesive model can be determined by comparing the calculated wavelength (λ_d) of the buckled ribbon with experimentally measured results. *SI Appendix*, Figs. S2 and S3, present values of γ and T_1^0 for the weak interfaces of 3 different film/substrate systems [epoxy (SU-8)/silicone (D-Skin), Si/D-Skin, and polyimide (PI)/D-Skin] examined in this study, as well as the strong interfaces. The results are shown in Table 1.

Consider a straight ribbon (length L_{weak} and width w, $w = L_{weak}/20$) that terminates with 2 square regions at the ends (side length $L_{strong} = 3w$) as bonding sites, where the target geometry for 3D assembly is an out-of-plane, arc-shaped structure. As the prestrain (ε_{pre}) in the elastomer substrate (D-Skin, Smooth-On) releases, the initial length ($L_0 = L_{weak} + L_{strong}$) changes to $L_1 = L_0/(1 + \varepsilon_{pre})$. The buckled ribbon is schematically shown in Fig. 1*B*. Here, a Cartesian coordinate system (x_1, x_2, x_3) has the axial direction of the ribbon along the x_1 axis and the thickness direction of the substrate along the x_3 axis. The buckle wavelength λ_d is defined as the straight distance between the 2 crack tips of the delaminated segment. The arc length of the delaminated segment is L_d^{film}. The proportion of the delaminated segment of the ribbon, i.e., L_d^{film}/L_{weak}, characterizes the state of delamination of the system. Fig. 1*C* provides a collection of experimental and computational results of this ratio (L_d^{film}/L_{weak}) for a SU-8 ribbon (thickness of 10 μm and length of 3 mm) assembled with a series of different prestrain (ε_{pre}).

Four regimes can be identified: wrinkling (regime I), partial delamination of the weak interface (regime II), full delamination of the weak interface (regime III), and partial delamination of the strong interface (regime IV), as marked by different colors in Fig. 1*C*. Regime III corresponds to the desired delamination state for 3D assembly, in this case to form an arc-shaped structure. Fig. 1*E*, Left, provides representative optical (colorized for improved contrast) images and corresponding FEA results for cases that represent these 4 regimes (marked as points b, c, d, and e in Fig. 1*C*). With a small level of prestrain release (e.g., $0 < \varepsilon_{pre} < 2.2\%$; regime I, marked as green), the ribbon undergoes wrinkling deformations with a wavelength ($\lambda_{wrinkle}$) of ∼845.1 μm, where the critical prestrain (∼0.08%) to trigger the wrinkling mode is very small, as a result of the large difference between the moduli of the film and the substrate. As the prestrain reaches a threshold value (∼2.2%), a region of delamination appears at the weak interface, leading to the formation of a buckled wave with a finite length (approximately a wrinkling wavelength). As a result, the delamination ratio (L_d^{film}/L_{weak}) jumps to a finite magnitude across this threshold prestrain, as reported in previous studies (47–49, 51, 52, 54). As the prestrain increases further ($2.2\% < \varepsilon_{pre} \leq 25.3\%$; regime II, marked as yellow in Fig. 1*C*), the delaminated segment enlarges rapidly, until the crack approaches the bonding sites, corresponding to full delamination of the weak interface.

Since the assembled structure approaches the design target when the delamination ratio reaches ∼90%, we regard the weak interface as fully delaminated when L_d^{film}/L_{weak} is above 90%. Beyond regime II, the ribbon/substrate system enters a relatively stable state, where the weak interface is fully delaminated and the strong interface is unperturbed. In this regime ($25.3\% < \varepsilon_{pre} \leq 62.4\%$; regime III, marked as blue in Fig. 1*C*), the delamination ratio changes very slightly (from 90% to 100%). As the prestrain exceeds another threshold (∼62.4%), delamination initiates at the strong interface, and propagates with a further increase in the prestrain, leading to a slow increase of the delamination ratio in this regime ($\varepsilon_{pre} > 62.4\%$; regime IV, marked as pink in Fig. 1*C*).

For relatively long ribbons, the delamination tends to initiate at multiple locations along the weak interface, giving rise to the formation of multiple buckled waves as the prestrain reaches the threshold (∼2.2%) to induce the crack initiation. Note that the example in Fig. 1*C* has a ribbon length of $\sim 3.5\lambda_{wrinkle}$, and the middle wrinkle has a larger amplitude than the other 2, due to the edge effect, thereby resulting in an initiation of delamination at the middle wrinkle. Fig. 1*D* shows results for delamination ratio (L_d^{film}/L_{weak}) for a SU-8 ribbon (thickness of 10 μm) with a length (8 mm) of $\sim 8.9\lambda_{wrinkle}$. In this condition, 2 deformation regimes can be identified, including wrinkling and partial delamination of the weak interface at 2 separated segments. Specifically, 2 buckled arches appear in both experiment and FEA as the prestrain exceeds ∼2.2% ($\varepsilon_{pre} > 2.2\%$; regime V, marked as gray in Fig. 1*D*). The 2 separated waves enlarge as the prestrain increases, but they do not converge into a single wave in the prestrain range of interest ($\varepsilon_{pre} \leq 100\%$). The result is a double-arch configuration [(h) in Fig. 1*E*]. Because this structure differs from the desired arc-shaped geometry, we do not further divide this regime (regime V), although delamination of strong interface occurs at large prestrains (e.g., >117%). For both single- and double-arch configurations, the delamination ratio (L_d^{film}/L_{weak}) and deformed ribbon configurations predicted by FEA agree very well with the experimental results, establishing FEA as a reliable design tool to achieve a desired delamination state of weak and strong interfaces.

Fig. 2 illustrates the utility of FEA in the construction of design diagrams that can facilitate choices of material/geometry-related parameters. Due to the random distribution of defects associated with film/substrate materials and interfaces, the location at which delamination of the weak interface occurs exhibits some experimental variability, as described in Fig. 2 *A* and *B* for an

Table 1. Calibration results of γ and T_1^0

Interface	Materials	γ (J/m^2)	T_1^0 (MPa)
Weak	SU-8/D-Skin	2.5	0.22
	Si/D-Skin	0.9	0.24
	PI/D-Skin	1.2	0.15
Strong	O-Si-O	4.5	0.42

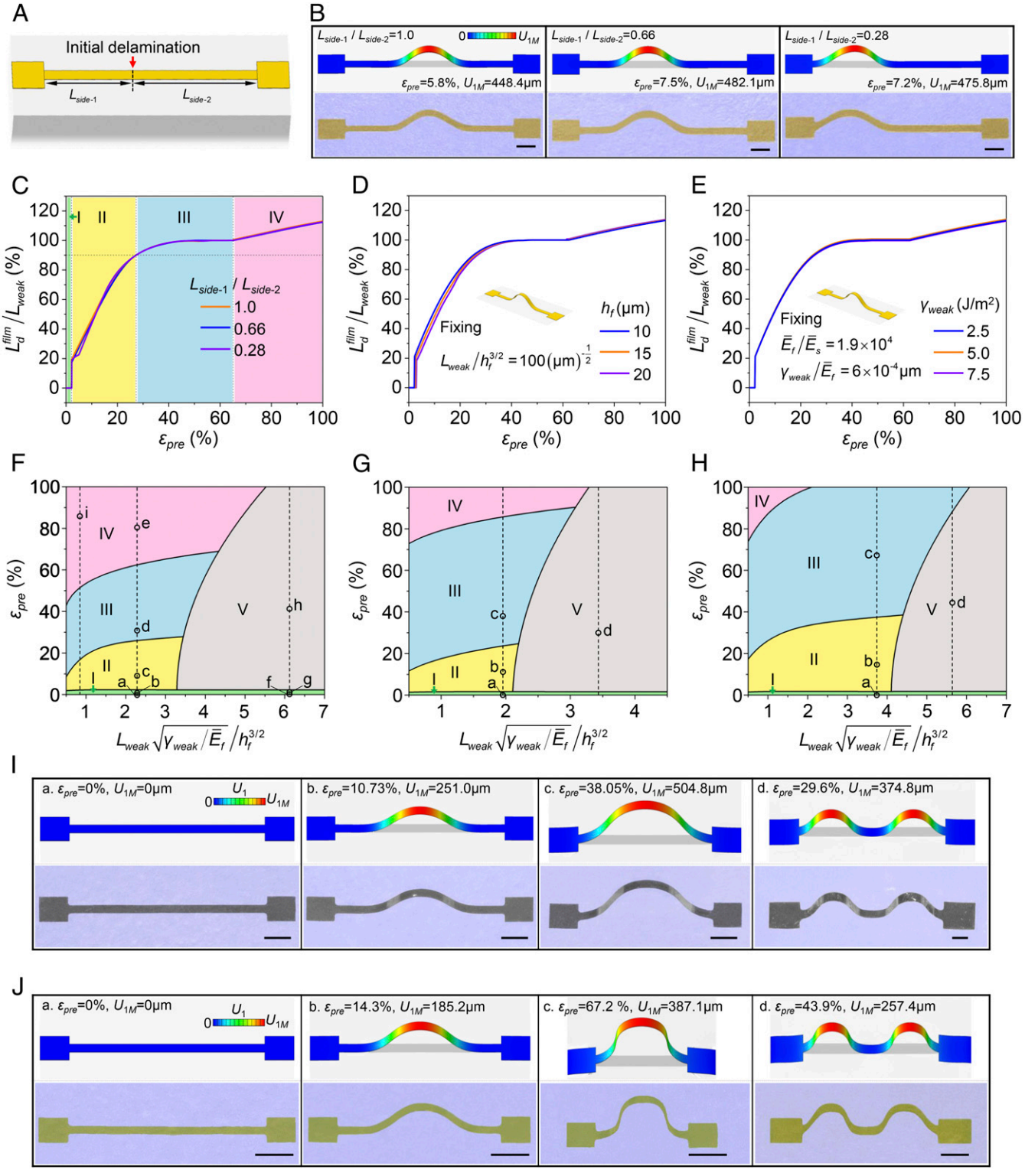

Fig. 2. Design diagram for the buckling-guided 3D assembly of straight ribbon mesostructures. (*A*) Illustration of the location at which delamination initiates. (*B*) Colorized experimental images and corresponding FEA predictions for 3 cases with different locations where delamination initiates. Here, L_{weak} = 4 mm and h_f = 10 μm. (*C*) FEA results on the evolution of the delamination ratio (L_d^{film}/L_{weak}) for the 3 cases shown in *B*. (*D*) Delamination ratio (L_d^{film}/L_{weak}) versus prestrain (ε_{pre}) for ribbons with 3 different film thicknesses (10, 15, and 20 μm), with fixed $L_{weak}/h_f^{3/2}$. (*E*) Similar results for ribbons with 3 different weak interface energies (2.5, 5.0, and 7.5 J/m^2), with fixed $\gamma_{weak}/\bar{E}_f$ and $\bar{E}_f/\bar{E}_s$. (*F–H*) Design diagrams for straight ribbon mesostructures in 3 different material systems, including SU-8/D-Skin in *F*, silicon/D-Skin in *G*, and PI/D-Skin in *H*. The colored regimes in the design diagrams represent wrinkling (green, regime I), partial delamination of the weak interface (yellow, regime II), full delamination of the weak interface (blue, regime III), partial delamination of the strong interface (pink, regime IV), and double-arc delamination of the weak interface (gray, regime V), respectively. (*I* and *J*) Colorized experimental images and FEA predictions of deformed configurations in the cases of silicon/D-Skin (in *I*) and PI/D-Skin (in *J*), corresponding to the design points marked in *G* and *H*, respectively. (Scale bars, 500 μm in *B* and 200 μm in *I* and *J*.)

SU-8 ribbon with the same geometry as that in Fig. 1*C*. The FEA results in Fig. 2 *A*–*C* show that the evolution of delamination ratio (L_d^{film}/L_{weak}) as well as the transition prestrains between different regimes are, however, insensitive to the location of delamination initiation. As such, we do not need to consider the effect of such an initiation location in the design diagram.

The key design parameters that affect the delamination process can be grouped into 3 classes, including the loading parameter (ε_{pre}), material parameters (interface energy γ_{weak} and elastic moduli, $\bar{E}_f$ and $\bar{E}_s$), and geometric parameters (film thickness h_f and length L_{weak}), where the subscripts f and s denote the film and substrate, respectively. The interface energy γ_{strong} is not taken into account herein, since most reports exploit strong covalent bonding at these interfaces. Inspired by the introduction by Bico et al. (55) of an elastocapillary length, $L_{ec} = h_f^{3/2}\sqrt{\bar{E}_f/(12\gamma)}$, as an important quantity that affects interface delamination, we define a dimensionless length of the weak interface as $\bar{L}_{weak} = \frac{L_{weak}}{h_f^{3/2}}\sqrt{\frac{\gamma_{weak}}{\bar{E}_f}} \propto \frac{L_{weak}}{L_{ec}}$, which incorporates the effects of γ_{weak}, $\bar{E}_f$, h_f, and L_{weak}. This scaling quantity is also consistent with the findings of Vella et al. (48, 49) and Zhang et al. (51), which indicate that the effects of these 4 parameters on the delamination process of hard/soft interface can be reflected in the form of a single combined parameter, $\bar{L}_{weak} = L_{weak}\sqrt{\gamma_{weak}/\bar{E}_f}/h_f^{3/2}$. The FEA results in Fig. 2 *D* and *E* and *SI Appendix*, Fig. S4, provide some additional support. In Fig. 2*D* and *SI Appendix*, Fig. S4*A*, the film/substrate systems of SU-8 and D-Skin with different film thicknesses h_f exhibit similar behaviors in the delamination ratio, by fixing the values of $L_{weak}/h_f^{3/2}$ and material parameters (γ_{weak}, $\bar{E}_f$, and $\bar{E}_s$) for both the cases of single- and double-arch modes. Similarly, the film/substrate systems of SU-8 and D-Skin with different interface energy γ_{weak} also display very similar responses in the delamination ratio, by fixing the values of $\gamma_{weak}/\bar{E}_f$, $\bar{E}_f/\bar{E}_s$, and geometric parameters (L_{weak} and h_f) (Fig. 2*E* and *SI Appendix*, Fig. S4*B*). Then the delamination ratio (L_d^{film}/L_{weak}) depends mainly on 3 dimensionless parameters, i.e., ε_{pre}, $L_{weak}\sqrt{\gamma_{weak}/\bar{E}_f}/h_f^{3/2}$, and $\bar{E}_f/\bar{E}_s$. For a specific film/substrate system, where the modulus ratio ($\bar{E}_f/\bar{E}_s$) is fixed, a design diagram related to the delamination state can be constructed in terms of the prestrain ε_{pre} and the dimensionless length, $\bar{L}_{weak} = L_{weak}\sqrt{\gamma_{weak}/\bar{E}_f}/h_f^{3/2}$.

Fig. 2*F* presents such a diagram for the SU-8/D-Skin material system, where the design points a through h correspond to the deformed configurations in Fig. 1*E*, and the design point i represents an almost fully delaminated state of the strong interface (*SI Appendix*, Fig. S5). The blue region represents the ideal delamination state desired in the 3D assembly process, i.e., full delamination of the weak interface and no delamination of the strong interface. The design diagram shows that the prestrain should lie in an optimal window for a prescribed dimensionless length, $\bar{L}_{weak} = L_{weak}\sqrt{\gamma_{weak}/\bar{E}_f}/h_f^{3/2}$, for example, $26.1\% < \varepsilon_{pre} < 62.4\%$ for $\bar{L}_{weak} = 3$. The lower bound of this window rises as $\bar{L}_{weak}$ increases, suggesting that a higher prestrain is needed to induce a full delamination of weak interface at a larger dimensionless length. Additionally, a large dimensionless length $\bar{L}_{weak}$ (e.g., >5.5) tends to give rise to the formation of a double-arch configuration. Fig. 2 *G* and *H* provide design diagrams for the Si/D-Skin and PI/D-Skin material systems. Experiments for selected design points [Si ribbon, $h_f = 1.5$ μm, $L_{weak} = 1.5$ mm in Fig. 2*G* (a–c) and 2.5 mm in Fig. 2*G* (d), and PI ribbon, $h_f = 3$ μm, $L_{weak} = 1$ mm in Fig. 2*H* (a–c) and 1.5 mm in Fig. 2*H* in (d)] marked in the diagrams yield configurations in Fig. 2 *I* and *J*. These results are in excellent agreement with FEA, and provide experimental evidence of the validity of the design diagrams. In comparison with SU-8 and Si ribbons, a higher level of prestrain is required to induce the full delamination of the weak interface in PI ribbons, which can be attributed to their lower modulus ratio ($\bar{E}_f/\bar{E}_s$). This finding is also consistent with experimental observations.

Design Diagrams for Buckling-Guided 3D Assembly of Helical Mesostructures. The design diagrams in Fig. 2 can be extended to other 2D precursor geometries. Fig. 3 provides examples for a representative class of 3D ribbon geometries, i.e., helical mesostructures that can be utilized in various applications as extremely stretchable interconnects (1, 56), tunable inductors (22), and flexible microswimmers with high motility (57). Here, a serpentine ribbon structure (Fig. 3*A* and *SI Appendix*, Fig. S6*A*) serves as the 2D precursor (Fig. 3*B*). A unit cell consists of 2 identical arc segments (arc angle, θ_0; radius, R_0; and width, $w = L_{weak}/20$) connected with 2 half circles (diameter, $D_{strong} = 2.5w$) that serve as the bonding sites. The total arc length of the weak interface and the span can be then given by ($L_{weak} = 2R_0\theta_0 - D_{strong}$) and [$L_{span0} = 4R_0\sin(\theta_0/2)$], respectively. Since this class of 2D precursor structure often consists of multiple (e.g., ≥4) unit cells, periodic boundary conditions (see *Methods* for details) along the compression direction can be exploited to reduce the computational cost. Fig. 3 *C*–*E* presents design diagrams for helical mesostructures formed with 3 representative arc angles (60°, 120°, and 180°), all in the SU-8/D-Skin material system. Experimental results confirm the delamination states at selected design points (a–e) marked in the diagrams, as shown in Fig. 3 *F*–*H*. The observations agree well with computational results, for both the wrinkling and buckling deformations.

These findings suggest that the delamination is increasingly difficult to initiate at the weak interfaces of helical mesostructures as the arc angle increases. Here, an increase in the angle increases the proportion of the serpentine ribbon (with $\theta_0 = 180°$) that is not closely aligned with the compression direction (x_3), where the substrate is stretched along the transverse direction (x_2) due to the Poisson effect, which could restrain the delamination. Owing to a similar curvature effect, a larger prestrain is required to induce full delamination of weak interface in the helical mesostructures than in the arch mesostructures (in Fig. 2*F*), especially at a large arc angle (e.g., 180°), for the same dimensionless length ($\bar{L}_{weak}$). Additionally, the boundary of single- and double-arch configurations shifts left with an increase in arc angle (θ_0), indicating that the double-arch mode is easier to stabilize for helical mesostructures with a larger arc angle. This behavior can be attributed to a weakened interaction between the 2 separated arches in the case of a larger arc angle. The dependence of the delamination ratio (L_d^{film}/L_{weak}) on the prestrain (ε_{pre}) appears in *SI Appendix*, Fig. S6 *B*–*D* for 3 typical designs with ($\theta_0 = 60°$, $\bar{L}_{weak} = 2.31$), ($\theta_0 = 120°$, $\bar{L}_{weak} = 1.54$), and ($\theta_0 = 180°$, $\bar{L}_{weak} = 1.15$). These results clearly show that a sharper transition of wrinkling to buckling mode occurs at $\theta_0 = 120°$ and 180°, since a higher level of prestrain is needed to induce such a transition.

In all experiments presented here, the release of prestrain in the substrate occurs slowly, corresponding to a quasi-static loading process. The interface properties, in particular, the interface energy, exhibit a significant dependence on loading rate, owing to the viscoelastic response of the elastomeric substrate (58). This rate dependence enables, in fact, a kinetically controlled mechanism for transfer printing (59–61), now widely used in hybrid flexible electronics, photovoltaics, displays, and other areas of microsystems technologies. Generally, the energy dissipation of interface separation typically increases with increasing the separation velocity. Based on this trend, the threshold prestrain

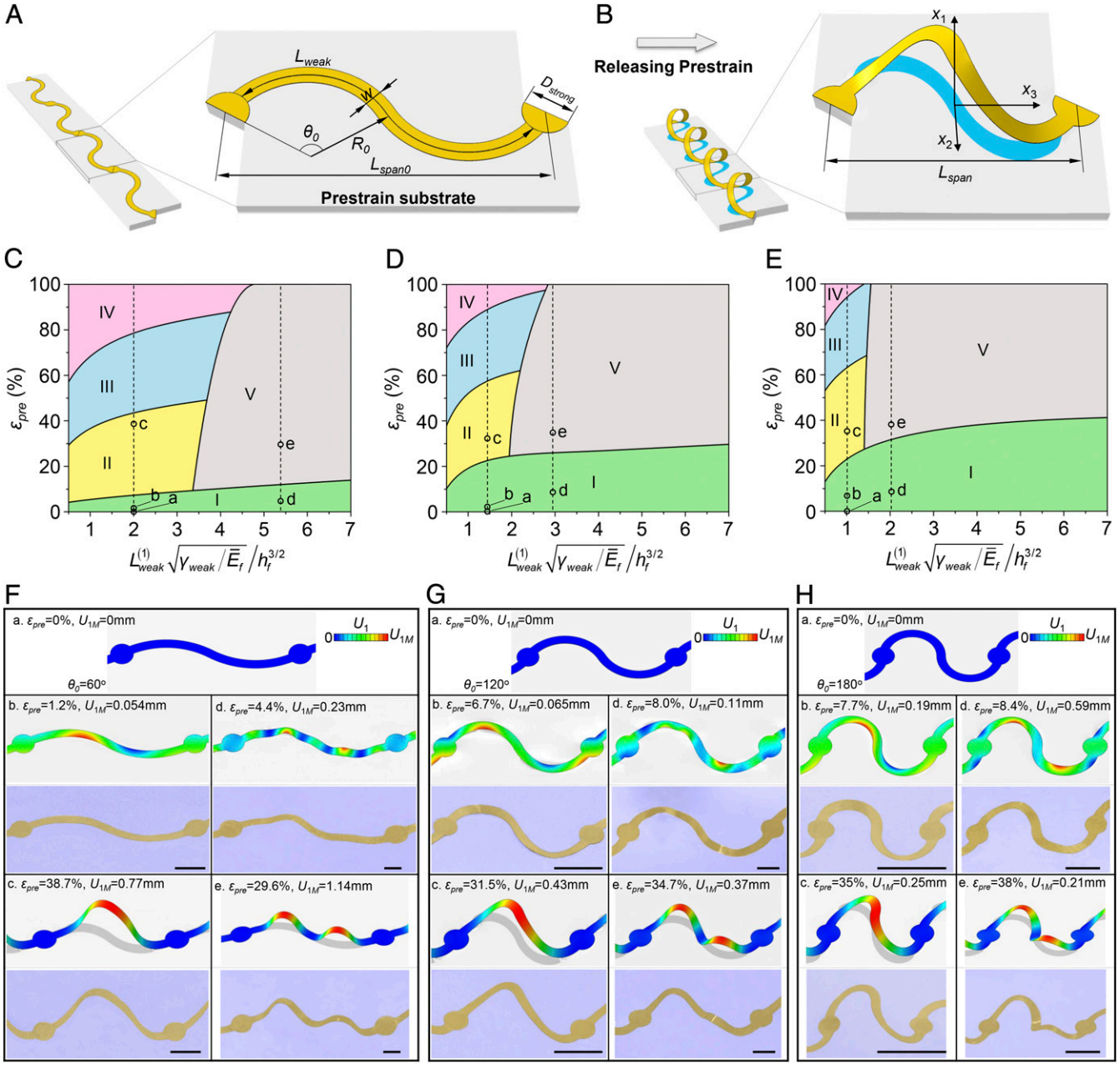

Fig. 3. Design diagram for the buckling-guided 3D assembly of helical mesostructures. (*A* and *B*) Computational model for FEA of serpentine ribbon mesostructures. (*C–E*) Design diagrams for helical mesostructures formed with 3 representative arc angles (60° in *C*, 120° in *D*, and 180° in *E*). The colored regimes in the diagrams represent wrinkling (green, regime I), partial delamination of the weak interface (yellow, regime II), full delamination of the weak interface (blue, regime III), partial delamination of the strong interface (pink, regime IV), and double-arc delamination of the weak interface (gray, regime V), respectively. (*F–H*) Colorized experimental images and FEA predictions of the deformed configurations for 3 different arc angles (60° in *F*, 120° in *G*, and 180° in *H*), corresponding to the design points marked in *C*, *D*, and *E*, respectively. (Scale bars, 500 μm.)

needed to induce full delamination of the weak interface will be increased with increasing release rate. Similarly, the delamination process also depends on the temperature, where the resulting thermal expansion mismatch between the film and substrate could be an additional factor.

Harnessing the Interface Mechanics to Achieve Reconfigurable 3D Mesostructures. Understanding interface delamination in the film/substrate system not only leads to improved engineering control, via avoidance of unwanted delamination states through rational design of 3D assembly, but also provides a versatile route to reconfigurable 3D mesostructures whose shapes can be changed and stabilized reversibly between distinct 3D geometries. Fig. 4*A* and *SI Appendix*, Fig. S7, present combined experimental and FEA results that illustrate the concept in the context of an H-shaped 2D precursor design. Here, reconfiguration occurs via control of the loading path, specifically the time sequence of release of biaxial prestrain. Fig. 4*A*, *Upper Middle* shows the SU-8 precursor structure, which consists of 3 straight ribbon components (2 of them with length $L^{(1)}_{weak}$ and 1 with length $L^{(2)}_{weak}$), integrated on a biaxially prestretched substrate (D-Skin; $\varepsilon_{prex2} = \varepsilon_{prex3} = 35\%$). The 4 square regions serve as the bonding sites. Appropriate choices of geometric

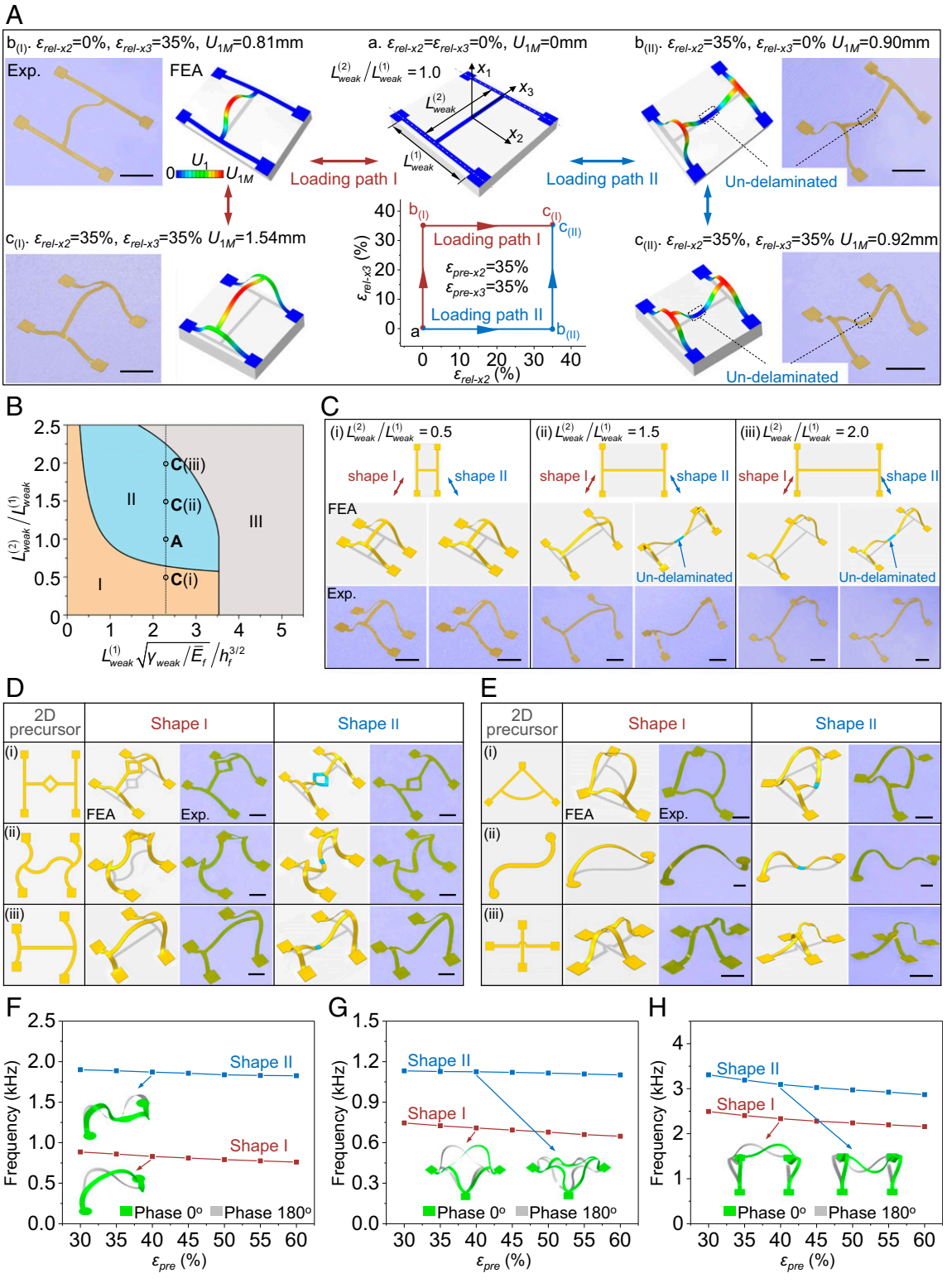

Fig. 4. Harnessing interface mechanics to achieve reconfigurable 3D mesostructures through loading-path controlled assembly. (*A*) Conceptual illustration of the strategy through a sequence of FEA results and a pair of colorized experimental images of reconfigurable 3D mesostructures (SU-8; 10 μm in thickness) based on an H-shaped precursor ($L^{(2)}_{weak}/L^{(1)}_{weak}$=1.0 and $\bar{L}^{(1)}_{weak}$= 2.31). (*B*) Design diagram for the assembly of reconfigurable 3D mesostructures from an H-shaped precursor. The colored regimes represent unique stable shapes (brown, regime I; gray, regime III) and bistable shapes (blue, regime II). (*C*) Colorized experimental images and FEA predictions for reconfigurable mesostructures (SU-8; 10 μm in thickness) with 3 representative length ratios (0.5 in *i*, 1.5 in *ii*, and 2.0 in *iii*), corresponding to the design points marked in *B*. (*D*) Three variants of H-shaped reconfigurable 3D mesostructures (PI; 15 μm in thickness). (*E*) A collection of reconfigurable 3D mesostructures (PI; 15 μm in thickness) with different geometries. (*F*) Resonant frequencies of the same vibrational mode for the 2 distinct shapes of the second design in *E*. *Insets* correspond to FEA images of the vibrational modes for the 2 distinct shapes with 40% prestrain, in which the amplitudes are magnified to clearly illustrate the modes. (*G* and *H*) Similar results for the first design in *E* and the design in *A*. (Scale bars, 1 mm.)

parameters (e.g., $\bar{L}^{(1)}_{weak} = \bar{L}^{(2)}_{weak} = 2.31$) ensure full delamination of ribbon along the x_3 direction after releasing the x_3-directional prestrain, in a manner similar to that of the buckling of a straight ribbon. Subsequent release of the prestrain along the x_2 direction then leads to the formation of a double-floor mesostructure (Fig. 1*A*, left bottom frame; following loading path I). Exchanging the order of sequential release of the prestrain changes the delamination process. Specifically, by releasing the prestrain along the x_2 direction, although the 2 ribbons along the x_2 direction fully delaminate, the central segment of the ribbon along the x_3 direction remains on the substrate (Fig. 1*A*, right top frame), due to the insufficient driving force to separate the interface at this region. During the release of the remnant prestrain along the x_3 direction, the pop-down configuration of the ribbon along the x_3 direction is very stable, as evidenced by the slight change of the delamination ratio for this ribbon (78.5% vs. 89.4%), as well as the energy landscape (see *SI Appendix*, Fig. S9 for details). The result of this sequential release (x_2 first and x_3 second) is a single-floor architecture with a pop-down mode for the central ribbon (Fig. 1*A*, right bottom frame; following loading path II). This single-floor architecture can be reshaped reversibly into the double-floor mesostructure in the left bottom frame by biaxially stretching the substrate to the flat configuration, followed by the sequential release with a different order (x_3 first and x_2 second). Previous experimental studies of this system (22), conducted without explicit consideration of the interface effects, report an unstable single-floor architecture, such that both simultaneous and sequential release lead to the double-floor configuration.

The bistability of the H-shaped precursor design depends on the prestrain (ε_{pre}), the dimensionless length ($\bar{L}^{(1)}_{weak} = L^{(1)}_{weak}\sqrt{\gamma_{weak}/\bar{E}_f}/h_f^{3/2}$), and the length ratio ($L^{(2)}_{weak}/L^{(1)}_{weak}$). For a representative biaxial prestrain (35%), a design diagram in terms of $L^{(2)}_{weak}/L^{(1)}_{weak}$ and $\bar{L}^{(1)}_{weak}$ can be constructed based on FEA, as shown in Fig. 4*B*. Design parameters in the brown, blue, and gray regions yield unique stable shapes, bistable shapes and double-/multiple-arch configurations through 2 different loading paths (I and II). For a small length ratio (e.g., $L^{(2)}_{weak}/L^{(1)}_{weak}$=0.5, $\bar{L}^{(1)}_{weak}$ = 2.31), the central ribbon, due to the short length, fully delaminates after release of the prestrain along the x_2 direction in loading path II (see *SI Appendix*, Fig. S9, for details). The result is a unique stable shape assembled through the different sequential release paths. The experimental results in Fig. 4 *A* and *C* (corresponding to the design points marked in Fig. 4*B*) agree with FEA predictions. When one of the ribbon components in the precursor structure exceeds a certain length (e.g., $L^{(2)}_{weak}/L^{(1)}_{weak}$= 1.0, $\bar{L}^{(1)}_{weak}$= 4.97), the assembly process yields 3D mesostructures with double- or multiple-arch configurations (see *SI Appendix*, Fig. S10 for details).

These design concepts can be exploited to achieve reconfigurable 3D mesostructures with a diversity of geometric configurations. A key advantage over those reported previously (32) is that preformed creases in the precursor are not needed, thereby simplifying the fabrication process and enhancing the yield. Fig. 4 *D* and *E* summarize a collection of examples, encompassing the results of experiments and FEA on distinct stable shapes. The designs in Fig. 4*D* correspond to variants of the H-shaped configuration, which mainly involve the replacement of straight ribbon components by curved ones. The first design in Fig. 4*E* adopts a curved triangular pattern, where the arc component exhibits pop-up and pop-down configurations during different release sequences (*SI Appendix*, Fig. S11). The second design in Fig. 4*E* incorporates a straight segment in a serpentine ribbon (θ_0 = 120°), thereby stabilizing the double-wave configuration during path II (x_2 first and x_3 second), in contrast to a helical configuration from path I (see *SI Appendix*, Fig. S12, for details). The last design exploits a double-layer design, where the top layer has a straight pattern, and the bottom layer has a circular hook design in the center. With appropriate geometric parameters, this design breaks the symmetry during the release of prestrain along the x_2 direction along path II (see *SI Appendix*, Fig. S13, for details), leading to the formation of an asymmetric 3D mesostructure.

The reconfigurable 3D mesostructures demonstrated above can be utilized in tunable MEMS whose resonance frequency can be adjusted between distinct values. Fig. 4 *F*–*H* demonstrates a set of simulation results that illustrate this capability. The differences in frequencies that result from this process are much higher than those achievable with a single geometry at different prestrains (62) for all of the cases studied herein. For example, Fig. 4*F* shows resonant frequencies of the same vibrational mode for 2 distinct shapes of the second design in Fig. 4*E*. In comparison with the helical shape (shape I), the double-wave shape (shape II) has one more site bonded with the substrate, and therefore offers a higher rigidity, giving rise to a substantially increased (e.g., more than twice for ε_{pre} = 60%) resonant frequency. By tuning the prestrain (e.g., from 30% to 60%) adopted in the assembly, the resonant frequency can be only changed by <15% (relatively) for both shapes. Fig. 4 *G* and *H* illustrates the dependence of the resonant frequency on prestrain for 2 stable shapes of the H-shaped design (Fig. 4*A*) and the curved triangular design (first one in Fig. 4*E*). These results also indicate a much higher range of frequency tunability than can be achieved through the 3D reconfiguration.

Conclusions

This work presents a systematic study of the delamination process involved in buckling-guided 3D assembly, through combined collection of FEA calculations and experimental measurements. The general design diagrams developed herein account for the influence of various geometric and materials parameters to provide guidelines for the optimal design of the assembly process. For example, the effect of curvature in 2D serpentine precursors retards the delamination of weak interface. This detailed understanding of interface mechanics allows access to structural bistable modes through a loading path strategy, as a versatile route to reconfigurable 3D mesostructures. Demonstrative examples show potential applications in reconfigurable MEMS whose resonant frequency can be adjusted between 2 distinct values. Exploring the utility of these reconfigurable mesostructures in mechanical energy harvesters, reconfigurable 3D antennas, and other devices appears to be a promising direction for future research.

Methods

Finite Element Analyses. Computational models of postbuckling analyses were developed using the finite element analysis software (ABAQUS) to simulate the processes of buckling-driven delamination during the release of prestrain in the substrate. Eight-node 3D solid elements (C3D8R) and 4-node shell elements (S4R) were used for the soft substrate and 2D precursors, respectively. Isotropic surface-based cohesive behavior with a bilinear traction–separation law (see *SI Appendix*, Fig. S1 *A* and *B* for details) was employed to model the interface between the 2D precursors and soft substrate. Convergence of mesh sizes was tested to ensure computational accuracy. For straight ribbon structures (Figs. 1 and 2) and reconfigurable ribbon structures (Fig. 4), in-plane displacement components were applied to the side surfaces of the computational model. For the serpentine ribbon structure consisting of multiple cells (Fig. 3*A*), periodic boundary conditions were implemented on the left and right faces of the unit cell to save the computational efforts. Focusing on pairs of nodes periodically located on the 2 faces, their displacements can be related by $U_3^{left} - U_3^{right} = (\varepsilon_{pre}/(1+\varepsilon_{pre}))L_{span0}$, $U_1^{left} - U_1^{right} = 0$, and $U_2^{left} - U_2^{right} = 0$, where the superscripts "right" and "left" denote the right and left faces of the unit cell. Linear perturbation analyses based on film/substrate systems determined the critical buckling modes that were implemented as initial imperfections in the postbuckling simulations to trigger the

wrinkling deformations. The wrinkling-to-delamination follows naturally in the simulations, without the need to introduce additional imperfections, except for the study on the effect of delamination location in Fig. 2 *A* and *B*. The post-buckling simulations were performed using conventional static analysis in ABAQUS. The hyperelastic behavior of substrate was described by the Mooney–Rivlin constitutive model, with material coefficients of $C_{10} = 0.023$, $C_{01} = 0.0057$, and $D_1 = 0.71$ in ABAQUS. The films were modeled using the linear elastic relations, with the elastic modulus (E) and Poisson's ratio (ν) given by $E_{SU8} = 4.02$ GPa and $\upsilon_{SU8} = 0.22$ for SU-8; $E_{Si} = 130$ GPa and $\upsilon_{Si} = 0.27$ for silicon; and $E_{PI} = 2.5$ GPa and $\upsilon_{PI} = 0.34$ for PI.

Fabrication Methods for 3D SU-8 Mesostructures. Preparation of 3D SU-8 mesostructures began with spin casting a layer of an adhesion promoter (30 nm; Omnicoat) on a silicon wafer, followed by a layer of SU-8 (10 μm), as shown in *SI Appendix*, Fig. S1. Photopatterning the SU-8 defined the geometries of the 2D precursors. Immersion in acetone removed the Omnicoat and released the precursors from the silicon wafer, which were then retrieved by a wafer-soluble tape (polyvinyl alcohol; 3M Co.). Selective deposition of a thin layer of Ti (5 nm) and SiO_2 (50 nm) onto targeted sites of the 2D precursors, followed by transfer printing the 2D precursors onto a soft silicone elastomer substrate (Dragon Skin; Smooth-On) that was prestrained and exposed to ozone, yielded strong interfaces only at the bonding sites. Slowly releasing the prestrain in the substrate completed the 3D assembly process.

Fabrication Methods for 3D Silicon Mesostructures. Preparation of 3D silicon mesostructures began with photolithography and reactive ion etching (RIE) of the top silicon layer (1.2 μm) on a silicon-on-insulator wafer. Immersion in hydrofluoric acid (HF) removed the buried oxide from the exposed regions and also under the edges of the patterned silicon. Transferring the precursors onto a polydimethylsiloxane stamp and then to a sheet of water-soluble tape prepared samples for 3D assembly. The remaining steps for 3D assembly followed procedures described above.

Fabrication Methods for 3D PI Mesostructures. Preparation of thin 3D PI mesostructures (Fig. 2 *H* and *J*) began with spin casting a layer of polymethyl methacrylate (PMMA) (50 nm) followed by a layer of PI (3 μm) on a silicon wafer. Photolithography and RIE patterned the PI into geometries of the 2D precursors. After removing the PMMA by immersion in acetone, the 2D precursors were retrieved with a water-soluble tape. The remaining steps for 3D assembly followed procedures described above.

Preparation of thick 3D PI mesostructures (Fig. 4 *D* and *E*) began with automated mechanical cutting of films of PI (15 μm). A water-soluble tape facilitated the retrieval of patterned PI films from the adhesive cutting mat to the soft silicone substrate. A commercial adhesive (Super Glue; Gorilla Glue Company) dispensed at desired locations on the 2D precursors resulted in a strong interface after curing for ∼5 min at room temperature. Releasing the prestrain in the substrate completed the 3D assembly process.

ACKNOWLEDGMENTS. The authors acknowledge the support from the Center for Bio-Integrated Electronics at Northwestern University. Yihui Zhang acknowledges support from the National Natural Science Foundation of China (nos. 11672152 and 11722217) and the Tsinghua National Laboratory for Information Science and Technology. Y.H. acknowledges the support from the NSF (nos. CMMI1534120 and CMMI1635443).

1. K.-I. Jang *et al.*, Self-assembled three dimensional network designs for soft electronics. *Nat. Commun.* **8**, 15894 (2017).
2. N. Zhou, C. Liu, J. A. Lewis, D. Ham, Gigahertz electromagnetic structures via direct ink writing for radio-frequency oscillator and transmitter applications. *Adv. Mater.* **29**, 1605198 (2017).
3. W. Lee *et al.*, Two-dimensional materials in functional three-dimensional architectures with applications in photodetection and imaging. *Nat. Commun.* **9**, 1417 (2018).
4. D. Bishop, F. Pardo, C. Bolle, R. Giles, V. Aksyuk, Silicon micro-machines for fun and profit. *J. Low Temp. Phys.* **169**, 386–399 (2012).
5. A. C. Siegel *et al.*, Foldable printed circuit boards on paper substrates. *Adv. Funct. Mater.* **20**, 28–35 (2010).
6. P. V. Braun, Materials chemistry in 3D templates for functional photonics. *Chem. Mater.* **26**, 277–286 (2014).
7. Z. Liu, *et al.*, Nano-kirigami with giant optical chirality. *Sci. Adv.* **4**, eaat4436 (2018).
8. X. Dai, W. Zhou, T. Gao, J. Liu, C. M. Lieber, Three-dimensional mapping and regulation of action potential propagation in nanoelectronics-innervated tissues. *Nat. Nanotechnol.* **11**, 776–782 (2016).
9. T. G. Leong *et al.*, Tetherless thermobiochemically actuated microgrippers. *Proc. Natl. Acad. Sci. U.S.A.* **106**, 703–708 (2009).
10. V. Magdanz, S. Sanchez, O. G. Schmidt, Development of a sperm-flagella driven micro-bio-robot. *Adv. Mater.* **25**, 6581–6588 (2013).
11. Z. Yan *et al.*, Three-dimensional mesostructures as high-temperature growth templates, electronic cellular scaffolds, and self-propelled microrobots. *Proc. Natl. Acad. Sci. U.S.A.* **114**, E9455–E9464 (2017).
12. S. Yao, P. Swetha, Y. Zhu, Nanomaterial-enabled wearable sensors for healthcare. *Adv. Healthc. Mater.* **7**, 1700889 (2018).
13. H. Ning *et al.*, Holographic patterning of high-performance on-chip 3D lithium-ion microbatteries. *Proc. Natl. Acad. Sci. U.S.A.* **112**, 6573–6578 (2015).
14. J. H. Pikul, H. Gang Zhang, J. Cho, P. V. Braun, W. P. King, High-power lithium ion microbatteries from interdigitated three-dimensional bicontinuous nanoporous electrodes. *Nat. Commun.* **4**, 1732 (2013).
15. H. Zhang, X. Yu, P. V. Braun, Three-dimensional bicontinuous ultrafast-charge and -discharge bulk battery electrodes. *Nat. Nanotechnol.* **6**, 277–281 (2011).
16. B. Y. Ahn *et al.*, Omnidirectional printing of flexible, stretchable, and spanning silver microelectrodes. *Science* **323**, 1590–1593 (2009).
17. M. A. Skylar-Scott, S. Gunasekaran, J. A. Lewis, Laser-assisted direct ink writing of planar and 3D metal architectures. *Proc. Natl. Acad. Sci. U.S.A.* **113**, 6137–6142 (2016).
18. R. L. Truby, J. A. Lewis, Printing soft matter in three dimensions. *Nature* **540**, 371–378 (2016).
19. L. L. Lebel, B. Aissa, M. A. El Khakani, D. Therriault, Ultraviolet-assisted direct-write fabrication of carbon nanotube/polymer nanocomposite microcoils. *Adv. Mater.* **22**, 592–596 (2010).
20. T. A. Schaedler *et al.*, Ultralight metallic microlattices. *Science* **334**, 962–965 (2011).
21. K. A. Arpin *et al.*, Multidimensional architectures for functional optical devices. *Adv. Mater.* **22**, 1084–1101 (2010).
22. S. Xu *et al.*, Assembly of micro/nanomaterials into complex, three-dimensional architectures by compressive buckling. *Science* **347**, 154–159 (2015).
23. X. Guo *et al.*, Two- and three-dimensional folding of thin film single-crystalline silicon for photovoltaic power applications. *Proc. Natl. Acad. Sci. U.S.A.* **106**, 20149–20154 (2009).
24. C. Py *et al.*, Capillary origami: Spontaneous wrapping of a droplet with an elastic sheet. *Phys. Rev. Lett.* **98**, 156103 (2007).
25. V. Y. Prinz *et al.*, A new technique for fabricating three-dimensional micro- and nanostructures of various shapes. *Nanotechnology* **12**, 399–402 (2001).
26. T. H. Ware, M. E. McConney, J. J. Wie, V. P. Tondiglia, T. J. White, Voxelated liquid crystal elastomers. *Science* **347**, 982–984 (2015).
27. C. Baek, P. M. Reis, Rigidity of hemispherical elastic gridshells under point load indentation. *J. Mech. Phys. Solids* **124**, 411–426 (2019).
28. C. Baek, A. O. Sageman-Furnas, M. K. Jawed, P. M. Reis, Form finding in elastic gridshells. *Proc. Natl. Acad. Sci. U.S.A.* **115**, 75–80 (2018).
29. J. Marthelot, F. L. Jimenez, A. Lee, J. W. Hutchinson, P. M. Reis, Buckling of a pressurized hemispherical shell subjected to a probing force. *J. Appl. Mech.* **84**, 121005 (2017).
30. R. Al-Rashed, F. López Jiménez, J. Marthelot, P. M. Reis, Buckling patterns in biaxially pre-stretched bilayer shells: Wrinkles, creases, folds and fracture-like ridges. *Soft Matter* **13**, 7969–7978 (2017).
31. J. Cui, F. R. Poblete, Y. Zhu, Origami/kirigami-guided morphing of composite sheets. *Adv. Funct. Mater.* **28**, 1802768 (2018).
32. H. Fu *et al.*, Morphable 3D mesostructures and microelectronic devices by multistable buckling mechanics. *Nat. Mater.* **17**, 268–276 (2018).
33. Y. Liu *et al.*, Guided formation of 3D helical mesostructures by mechanical buckling: Analytical modeling and experimental validation. *Adv. Funct. Mater.* **26**, 2909–2918 (2016).
34. Z. Yan *et al.*, Mechanical assembly of complex, 3D mesostructures from releasable multilayers of advanced materials. *Sci. Adv.* **2**, e1601014 (2016).
35. Z. Yan *et al.*, Controlled mechanical buckling for origami-inspired construction of 3D microstructures in advanced materials. *Adv. Funct. Mater.* **26**, 2629–2639 (2016).
36. Y. Zhang *et al.*, A mechanically driven form of Kirigami as a route to 3D mesostructures in micro/nanomembranes. *Proc. Natl. Acad. Sci. U.S.A.* **112**, 11757–11764 (2015).
37. H. Luan *et al.*, Design and fabrication of heterogeneous, deformable substrates for the mechanically guided 3D assembly. *ACS Appl. Mater. Interfaces* **11**, 3482–3492 (2019).
38. X. Wang *et al.*, Freestanding 3D mesostructures, functional devices, and shape-programmable systems based on mechanically induced assembly with shape semory polymers. *Adv. Mater.* **31**, 1805615 (2019).
39. M. Han *et al.*, Three-dimensional piezoelectric polymer microsystems for vibrational energy harvesting, robotic interfaces and biomedical implants. *Nat Electron* **2**, 26–35 (2019).
40. B. H. Kim *et al.*, Mechanically guided post-assembly of 3D electronic systems. *Adv. Funct. Mater.* **28**, 1803149 (2018).
41. F. Liu *et al.*, High performance, tunable electrically small antennas through mechanically guided 3D assembly. *Small* **15**, e1804055 (2019).
42. K. Nan *et al.*, Soft three-dimensional microscale vibratory platforms for characterization of nano-thin polymer films. *ACS Nano* **13**, 449–457 (2019).
43. H. Fu *et al.*, Mechanically-guided deterministic assembly of 3D mesostructures assisted by residual stresses. *Small* **13**, 1700151 (2017).
44. H. H. Yu, J. W. Hutchinson, Influence of substrate compliance on buckling delamination of thin films. *Int. J. Fract.* **113**, 39–55 (2002).
45. G. Parry *et al.*, Effect of substrate compliance on the global unilateral post-buckling of coatings: AFM observations and finite element calculations. *Acta Mater.* **53**, 441–447 (2005).
46. S. Goyal, K. Srinivasan, G. Subbarayan, T. Siegmund, On instability-induced debond initiation in thin film systems. *Eng. Fract. Mech.* **77**, 1298–1313 (2010).

47. H. Mei, C. M. Landis, R. Huang, Concomitant wrinkling and buckle-delamination of elastic thin films on compliant substrates. *Mech. Mater.* **43**, 627–642 (2011).
48. D. Vella, J. Bico, A. Boudaoud, B. Roman, P. M. Reis, The macroscopic delamination of thin films from elastic substrates. *Proc. Natl. Acad. Sci. U.S.A.* **106**, 10901–10906 (2009).
49. T. J. W. Wagner, D. Vella, The 'Sticky Elastica': Delamination blisters beyond small deformations. *Soft Matter* **9**, 1025–1030 (2013).
50. O. Oshri, Y. Liu, J. Aizenberg, A. C. Balazs, Delamination of a thin sheet from a soft adhesive Winkler substrate. *Phys. Rev. E* **97**, 062803 (2018).
51. Q. Zhang, Y. Jie, Spontaneous buckling-driven periodic delamination of thin films on soft substrates under large compression. *J. Mech. Phys. Solids* **118**, 40–57 (2018).
52. K. Pan, Y. Ni, L. He, R. Huang, Nonlinear analysis of compressed elastic thin films on elastic substrates: From wrinkling to buckle-delamination. *Int. J. Solids Struct.* **51**, 3715–3726 (2014).
53. R. Boijoux, G. Parry, J. Y. Faou, C. Coupeau, How soft substrates affect the buckling delamination of thin films through crack front sink-in. *Appl. Phys. Lett.* **110**, 141602 (2017).
54. A. J. Nolte, J. Young Chung, C. S. Davis, C. M. Stafford, Wrinkling-to-delamination transition in thin polymer films on compliant substrates. *Soft Matter* **13**, 7930–7937 (2017).
55. J. Bico, B. Roman, L. Moulin, A. Boudaoud, Adhesion: Elastocapillary coalescence in wet hair. *Nature* **432**, 690 (2004).
56. Y. Ling *et al.*, Mechanically assembled, three-dimensional hierarchical structures of cellular graphene with programmed geometries and outstanding electromechanical properties. *ACS Nano* **12**, 12456–12463 (2018).
57. H. W. Huang *et al.*, Adaptive locomotion of artificial microswimmers. *Sci. Adv.* **5**, eaau1532 (2019).
58. E. Barthel, S. Roux, Velocity-dependent adherence: An analytical approach for the JKR and DMT models. *Langmuir* **16**, 8134–8138 (2000).
59. M. A. Meitl *et al.*, Transfer printing by kinetic control of adhesion to an elastomeric stamp. *Nat. Mater.* **5**, 33–38 (2006).
60. X. Feng *et al.*, Competing fracture in kinetically controlled transfer printing. *Langmuir* **23**, 12555–12560 (2007).
61. A. Carlson, A. M. Bowen, Y. Huang, R. G. Nuzzo, J. A. Rogers, Transfer printing techniques for materials assembly and micro/nanodevice fabrication. *Adv. Mater.* **24**, 5284–5318 (2012).
62. X. Ning *et al.*, Three-dimensional multiscale, multistable, and geometrically diverse microstructures with tunable vibrational dynamics assembled by compressive buckling. *Adv. Funct. Mater.* **27**, 1605914 (2017).